Article

Indentation of Anisotropic Tissue Using a Three-Dimensional Mechanical Bidomain Model

Dilmini Wijesinghe [1],* and Bradley J. Roth [2]

1   USC Mark and Mary Stevens Neuroimaging and Informatics Institute, Los Angeles, CA 90033, USA
2   Department of Physics, Oakland University, Rochester, MI 48309, USA
*   Correspondence: dwijesinghe@ini.usc.edu

Abstract: Computation-based mathematical models of tissue indentation are capable of predicting the distribution of forces and mechanical properties of soft tissues. This paper presents a three-dimensional mathematical model of anisotropic tissue indentation developed using the mechanical bidomain model. The mechanical bidomain model hypothesizes that the relative displacement between intra- and extracellular spaces triggers a force on the mechanosensitive proteins in the membrane: integrins. Some soft tissues, such as cardiac muscle, are anisotropic, a property which arises from the fibrous structure of the tissue. The degree of anisotropy in intra- and extracellular spaces can be different. Tissue indentation for different anisotropy ratios that indicate isotropy, equal anisotropy and unequal anisotropy, were tested using the model. Results of the tissue indentation analysis compared the spatial distribution of the magnitude of bidomain displacement for different anisotropy conditions between monodomain and bidomain models. The proposed mathematical model predicted unexpected spatial patterns of cardiac mechanotransduction for unequal anisotropy ratios of mechanical modulus.

Keywords: cardiac tissue; mechanotransduction; three-dimensional mathematical modeling; tissue indentation; anisotropy

1. Introduction

Tissue abnormalities and changes in regional loading or maladaptation of myocardial tissue can contribute to the growth and remodeling of the heart. Long-term effects such as this can lead to apoptosis and diseases such as cardiac hypertrophy. Concomitantly, soft tissues, including cardiac tissue, are heterogeneous, nearly incompressible, and anisotropic, where the anisotropy arises from the underlying muscle fibers. Such tissues have complex geometries, and often are subject to large deformations [1,2]. Therefore, analyzing mechanical behavior and deformations of anisotropic tissue is vital and challenging due to its complex nature.

Indentation is a widely used technique in biomechanics to analyze the mechanical behavior and properties of soft tissue [3,4]. Due to the complex nature of the mechanical problems arising in traditional indentation tests on soft tissues, numerical techniques can provide an alternative way of analyzing the mechanical behavior of soft tissues on both cellular and regional scales [5]. They also can predict what mechanotransduction occurs during indentation: how the indenter pressing on the tissue causes it to grow and remodel.

This paper presents a finite difference analysis of indentation of anisotropic tissue using the mechanical bidomain model, a macroscopic mathematical model based on the microscopic properties of the tissue. As an example, we take the tissue to be cardiac muscle, but we do not stress specific parameter values because the model should apply qualitatively to a variety of soft tissues (e.g., cartilage).

The mechanical bidomain model accounts for the fiber-based anisotropy in both intra- and extracellular spaces and assumes that each can have different degrees of anisotropy

(unequal anisotropy ratios). In 2019, a 2D mechanical bidomain model was implemented that included these properties of anisotropy [6]. In our derivation of the 3D mechanical bidomain model, we extended the equations of the 2D model with anisotropic properties.

Another reason for choosing this study of tissue indentation is that it is analogous to unipolar electrical stimulation of cardiac tissue, where current is injected through a small electrode. In 1989, Sepulveda et al. used the electrical bidomain model to show that unequal anisotropy ratios are critical to understanding unipolar stimulation, and the insights gained from that study carried over to analyzing pacing and defibrillation of the heart [7].

Over the past decade, the mechanical bidomain model was developed as a two-dimensional (2D) model and it was able to successfully address unresolved questions in the growth and remodeling of soft tissue [8,9]. The most significant difference between the mechanical bidomain model and other monodomain models that are currently available, is that the mechanical bidomain model can distinguish the mechanical properties in the intra- and extracellular spaces of cardiac tissue. Our hypothesis is that differences in the intra- and extracellular displacements activate integrins and thereby drive mechanotransduction. In this paper we developed a three-dimensional numerical implementation of the mechanical bidomain model to simulate tissue indentation.

2. Materials and Methods

2.1. Derivation of Analytical Equations

We considered a 3D cube of anisotropic cardiac tissue. The word 'bidomain' describes the two domains: intracellular space (denoted by the subscript '*i*') and extracellular space (denoted by the subscript '*e*'). The intra- and extracellular spaces are coupled by membrane proteins such as integrins. The intracellular space, extracellular space, and integrins are represented by sets of mechanical springs that obey Hooke's law (Figure 1).
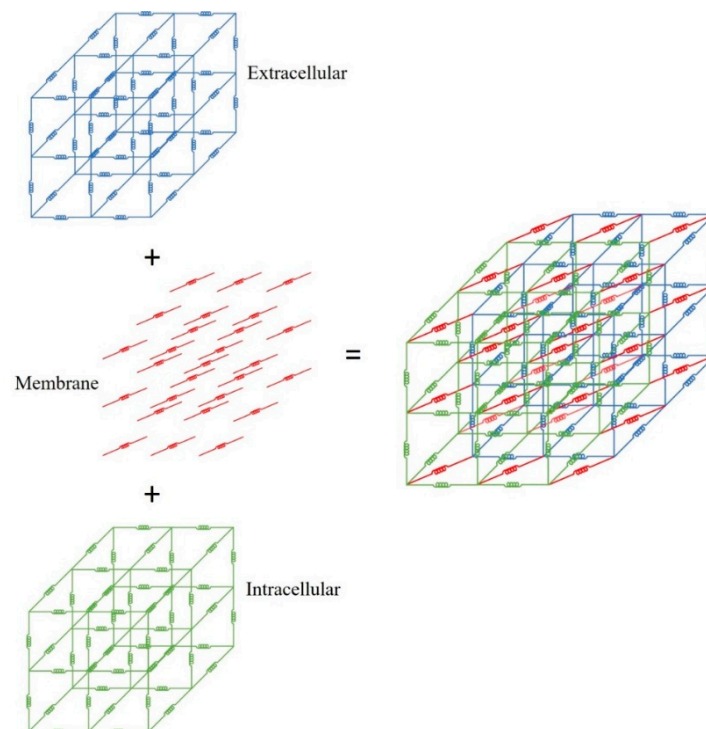
Figure 1. Three dimensional mechanical bidomain model. The networks of mechanical springs represent the mechanical properties of intracellular space (green), extracellular space (blue), and integrins in the membrane (red).

The displacements of the intra- and extracellular spaces are denoted by **u** and **w**. The different mechanical properties of the intra- and extracellular spaces are represented by two shear moduli, ν (for intracellular space) and μ (for extracellular space). To indicate the anisotropic properties of the tissue, we include an additional modulus along the direction of the fibers (the x direction) for both intra- and extracellular spaces, γ_i and γ_e. The pressures in intracellular and extracellular spaces are denoted by p and q. The equations of the mechanical bidomain model are derived using the stress (τ) and strain (ε) tensors. The stress–strain relations for the intracellular and extracellular space are:

$$\boldsymbol{\tau}_i = -p\,\mathbf{I} + 2\nu\,\boldsymbol{\varepsilon}_i + \gamma_i\,\varepsilon_{ixx}\,\hat{\mathbf{i}}, \tag{1}$$

$$\boldsymbol{\tau}_e = -q\,\mathbf{I} + 2\mu\boldsymbol{\varepsilon}_e + \gamma_e\,\varepsilon_{exx}\,\hat{\mathbf{i}}. \tag{2}$$

Consider a displacement vector x defined in a Euclidian space denoted by $\mathbf{x} = \{x_1,\ x_2,\ x_3\}$. The relation between linear strains and displacements, **u** and **w** can be written as:

$$\varepsilon_i = \frac{1}{2}\ (\mathbf{u}\nabla_{\mathbf{x}} + \nabla_{\mathbf{x}}\mathbf{u}), \tag{3}$$

$$\varepsilon_e = \frac{1}{2}\ (\mathbf{w}\nabla_{\mathbf{x}} + \nabla_{\mathbf{x}}\mathbf{w}). \tag{4}$$

The three-dimensional equations for mechanical equilibrium in both the intra- and extracellular spaces are:

$$\nabla\!\cdot\!\boldsymbol{\tau}_i = K(\mathbf{u} - \mathbf{w}), \tag{5}$$

$$\nabla\!\cdot\!\boldsymbol{\tau}_e = -K(\mathbf{u} - \mathbf{w}). \tag{6}$$

The parameter K represents the spring constant of the coupling between intra- and extracellular spaces.

By substituting Equations (1)–(4) into the equations of mechanical equilibrium (Equations (5) and (6)) and setting the divergence of the displacements to zero, we obtain:

$$-\nabla p + \nu\nabla^2\mathbf{u} + \gamma_i\,\frac{\partial^2 u_x}{\partial x^2}\hat{\mathbf{i}} = K(\mathbf{u} - \mathbf{w}), \tag{7}$$

$$-\nabla q + \mu\nabla^2\mathbf{w} + \gamma_e\,\frac{\partial^2 w_x}{\partial x^2}\hat{\mathbf{i}} = -K(\mathbf{u} - \mathbf{w}). \tag{8}$$

We can rewrite Equations (7) and (8) without pressure terms by taking the curl of the two equations as:

$$\nu\,\nabla^2(\nabla \times \mathbf{u}) - \gamma_i\,\frac{\partial^2}{\partial x^2}\left(\frac{\partial u_x}{\partial y}\,\hat{\mathbf{k}} + \frac{\partial u_x}{\partial z}\,\hat{\mathbf{j}}\right) = K(\nabla \times \mathbf{u} - \nabla \times \mathbf{w}), \tag{9}$$

$$\mu\,\nabla^2(\nabla \times \mathbf{w}) - \gamma_e\,\frac{\partial^2}{\partial x^2}\left(\frac{\partial w_x}{\partial y}\,\hat{\mathbf{k}} + \frac{\partial w_x}{\partial z}\,\hat{\mathbf{j}}\right) = -K(\nabla \times \mathbf{u} - \nabla \times \mathbf{w}). \tag{10}$$

Next, we introduce monodomain (**m**), and bidomain (**b**), displacements:

$$\mathbf{m} = \mathbf{u} + \left(\frac{\mu}{\nu}\right)\mathbf{w}, \tag{11}$$

$$\mathbf{b} = \mathbf{u} - \mathbf{w}. \tag{12}$$

The weighted sum of the displacements of the intra- and extracellular spaces, **m**, represents the monodomain behavior, and the difference of the displacements of the two spaces, **b**, represents the bidomain behavior [10]. The bidomain term indicates the force or torque

acting on integrins which triggers mechanotransduction. We can introduce new expressions for the displacements **u** and **w** using **m** and **b**, by solving Equations (11) and (12) as:

$$\mathbf{u} = \frac{\nu}{(\mu + \nu)} \left(\mathbf{m} + \frac{\mu}{\nu}\mathbf{b} \right),$$

(13)

$$\mathbf{w} = \frac{\nu}{(\mu + \nu)} (\mathbf{m} - \mathbf{b}).$$

(14)

When we express Equations (9) and (10) in terms of **m** and **b** we obtain:

$$\nabla^2(\nabla \times \mathbf{m}) + \frac{(\gamma_i + \gamma_e)}{(\mu + \nu)} \left(\frac{\partial^3 m_x}{\partial x^2 \partial z} \hat{\mathbf{j}} + \frac{\partial^3 m_x}{\partial x^2 \partial y} \hat{\mathbf{k}} \right) + \frac{(\mu\gamma_i - \nu\gamma_e)}{\nu(\mu + \nu)} \left(\frac{\partial^3 b_x}{\partial x^2 \partial z} \hat{\mathbf{j}} + \frac{\partial^3 b_x}{\partial x^2 \partial y} \hat{\mathbf{k}} \right) = 0,$$

(15)

$$\nabla^2(\nabla \times \mathbf{b}) + \frac{(\mu^2\gamma_i + \nu^2\gamma_e)}{\nu\mu(\mu + \nu)} \left(\frac{\partial^3 b_x}{\partial x^2 \partial z} \hat{\mathbf{j}} + \frac{\partial^3 b_x}{\partial x^2 \partial y} \hat{\mathbf{k}} \right) + \frac{(\mu\gamma_i - \nu\gamma_e)}{\mu(\mu + \nu)} \left(\frac{\partial^3 m_x}{\partial x^2 \partial z} \hat{\mathbf{j}} + \frac{\partial^3 m_x}{\partial x^2 \partial y} \hat{\mathbf{k}} \right) = K \frac{(\mu + \nu)}{\nu\mu} (\nabla \times \mathbf{b}).$$

(16)

We considered an incompressible tissue since tissue mostly consists of water. Therefore, displacements of the intra -and extracellular spaces have zero-divergence. The usual way of solving the 2D incompressible mechanical bidomain model is by using stream functions [6,11]. However, in the 3D model we generalize the 2D stream functions in 3D to vector potentials. Since the tissue is incompressible, the divergence of displacement **m** is zero. We set displacement **m** to have zero divergence by taking advantage of the vector identity that the divergence of the curl is zero as:

$$\mathbf{m} = \nabla \times \mathbf{M},$$

(17)

$$\mathbf{b} = \nabla \times \mathbf{B}.$$

(18)

M and **B** are vector potentials [12]. The displacements **m** and **b** depend on **M** and **B** only. We imposed the condition that the vector potentials of **M** and **B** are themselves divergenceless (a gauge condition [13]).

We define a set of non-dimensional parameters:

$$X = \frac{x}{D}, \quad Y = \frac{y}{D} \quad \text{and } \varepsilon = \frac{\mu\nu}{K(\mu + \nu)\, D^2}.$$

(19)

The expression for ε is how the coupling constant K is included in the equations. The term ε is also equal to σ^2/D^2, where σ is the new characteristic length constant introduced by the bidomain model and D is the length of the cube. By replacing **m** and **b** with **M** and **B**, using the vector identity $\nabla \times (\nabla \times \mathbf{M}) = \nabla(\nabla \cdot \mathbf{M}) - \nabla^2 \mathbf{M}$, and setting $\nabla \cdot \mathbf{M} = 0$ we obtain:

$$\nabla^4\mathbf{M} - \frac{(\gamma_i + \gamma_e)}{(\mu + \nu)} \left[\frac{\partial^3}{\partial X^2 \partial Z} \left(\frac{\partial M_z}{\partial Y} - \frac{\partial M_y}{\partial Z} \right)\hat{\mathbf{j}} - \frac{\partial^3}{\partial X^2 \partial Y} \left(\frac{\partial M_z}{\partial Y} - \frac{\partial M_y}{\partial Z} \right)\hat{\mathbf{k}} \right] - \frac{(\mu\gamma_i - \nu\gamma_e)}{\nu(\mu + \nu)} \left[\frac{\partial^3}{\partial X^2 \partial Z} \left(\frac{\partial B_z}{\partial Y} - \frac{\partial B_y}{\partial Z} \right)\hat{\mathbf{j}} - \frac{\partial^3}{\partial X^2 \partial Y} \left(\frac{\partial B_z}{\partial Y} - \frac{\partial B_y}{\partial Z} \right)\hat{\mathbf{k}} \right] = 0,$$

(20)

$$\nabla^4\mathbf{B} - \frac{(\mu^2\gamma_i + \nu^2\gamma_e)}{\nu\mu(\mu + \nu)} \left[\frac{\partial^3}{\partial X^2 \partial Z} \left(\frac{\partial B_z}{\partial Y} - \frac{\partial B_y}{\partial Z} \right)\hat{\mathbf{j}} - \frac{\partial^3}{\partial X^2 \partial Y} \left(\frac{\partial B_z}{\partial Y} - \frac{\partial B_y}{\partial Z} \right)\hat{\mathbf{k}} \right] - \frac{(\mu\gamma_i - \nu\gamma_e)}{\nu(\mu + \nu)} \left[\frac{\partial^3}{\partial X^2 \partial Z} \left(\frac{\partial M_z}{\partial Y} - \frac{\partial M_y}{\partial Z} \right)\hat{\mathbf{j}} - \frac{\partial^3}{\partial X^2 \partial Y} \left(\frac{\partial M_z}{\partial Y} - \frac{\partial M_y}{\partial Z} \right)\hat{\mathbf{k}} \right] = \frac{1}{\varepsilon} \nabla^2\mathbf{B}.$$

(21)

For an isotropic tissue ($\gamma_i = \gamma_e = 0$), all the extra terms on the left-hand side are zero and Equations (20) and (21) uncouple, becoming simply:

$$\nabla^4\mathbf{M} = 0,$$

(22)

$$\nabla^4\mathbf{B} = \frac{1}{\varepsilon} \nabla^2\mathbf{B}.$$

(23)

For tissue with equal anisotropy ratios $\left(\frac{\gamma_i}{\nu} = \frac{\gamma_e}{\mu}\right)$, Equations (20) and (21) remain uncoupled and become:

$$\nabla^4 \mathbf{M} - \frac{(\gamma_i + \gamma_e)}{(\mu + \nu)}\left[\frac{\partial^3}{\partial X^2 \partial Z}\left(\frac{\partial M_z}{\partial Y} - \frac{\partial M_y}{\partial Z}\right)\hat{\mathbf{j}} - \frac{\partial^3}{\partial X^2 \partial Y}\left(\frac{\partial M_z}{\partial Y} - \frac{\partial M_y}{\partial Z}\right)\hat{\mathbf{k}}\right] = 0, \quad (24)$$

$$\nabla^4 \mathbf{B} - \frac{(\mu^2 \gamma_i + \nu^2 \gamma_e)}{\nu\mu(\mu + \nu)}\left[\frac{\partial^3}{\partial X^2 \partial Z}\left(\frac{\partial B_z}{\partial Y} - \frac{\partial B_y}{\partial Z}\right)\hat{\mathbf{j}} - \frac{\partial^3}{\partial X^2 \partial Y}\left(\frac{\partial B_z}{\partial Y} - \frac{\partial B_y}{\partial Z}\right)\hat{\mathbf{k}}\right] = \frac{1}{\varepsilon}\nabla^2 \mathbf{B}. \quad (25)$$

The exact form of the expression for **m** in Equation (11) was selected to ensure the equations would uncouple in this case. The only situation leading to a coupling of **M** and **B** would be when the tissue has unequal anisotropy ratios $\left(\frac{\gamma_i}{\nu} \neq \frac{\gamma_e}{\mu}\right)$ and in the boundary conditions.
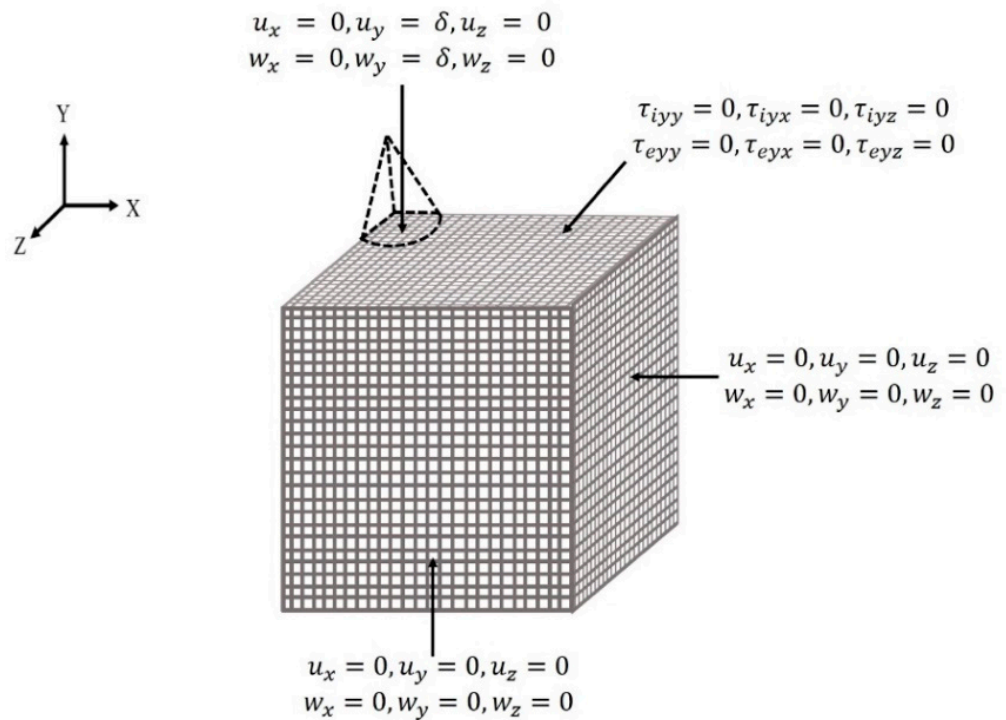
2.2. Boundary Conditions

We chose a cone-shaped indenter for the indentation of the tissue (Figure 2). By choosing a cone-shaped indenter, we were able to simplify the analysis by minimizing the contact zones occurring at the sides of the indenter and by limiting the contact zone to occur only at the bottom surface of the indenter.

(a)　　　　　　　　　　　　　(b)
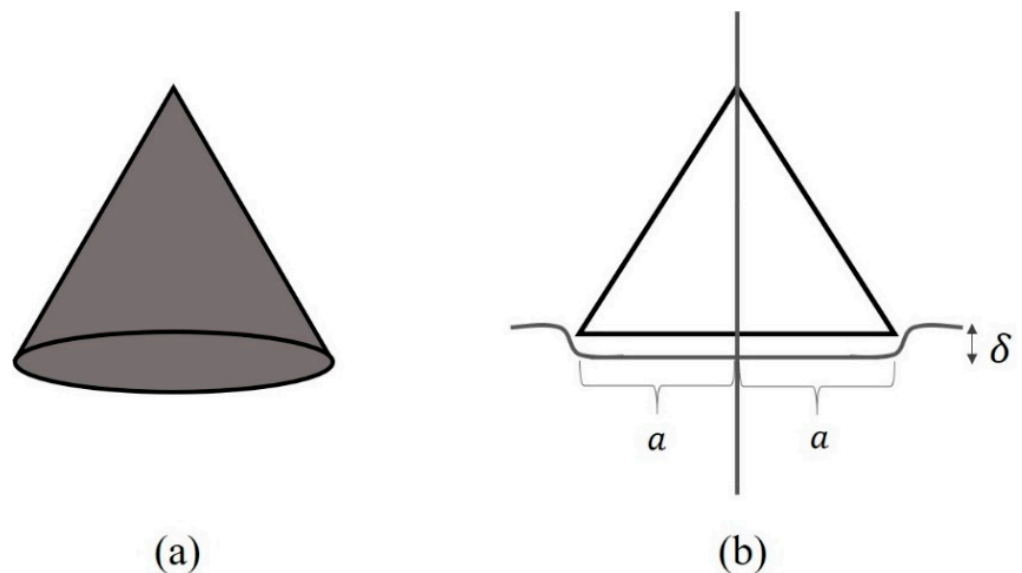
Figure 2. (**a**) Shape of the indenter. We chose a cone shaped indenter where only the bottom surface was in contact with the surface of the tissue. (**b**) Front view of the contact zone. Depth of the indentation is denoted by δ. Diameter of the base of the indenter is $2a$.

We considered the depth of indentation as infinitesimal in comparison with the dimensions of the tissue. This eliminates the effects at the boundaries $X = 1$ and $Z = 1$ (Figure 3). Additionally, as for the $Y = 1$ surface where indentation takes place, we considered a free boundary everywhere except under the indenter (Figure 3).

Due to the symmetry, boundary conditions were determined only for the $X = 1$, $Y = 1$, and $Z = 1$ surfaces (Figure 3). On the $Y = 1$ surface, the area away from the indenter is considered as a free boundary. Therefore, boundary conditions can be categorized into four sections: boundary conditions on the $Y = 1$ surface under the indenter, boundary conditions on the $Y = 1$ surface away from the indenter, boundary conditions on the $X = 1$ surface, and boundary conditions on the $Z = 1$ surface (Figure 3).

$$u_x = 0, u_y = \delta, u_z = 0$$
$$w_x = 0, w_y = \delta, w_z = 0$$

$$\tau_{iyy} = 0, \tau_{iyx} = 0, \tau_{iyz} = 0$$
$$\tau_{eyy} = 0, \tau_{eyx} = 0, \tau_{eyz} = 0$$

$$u_x = 0, u_y = 0, u_z = 0$$
$$w_x = 0, w_y = 0, w_z = 0$$

$$u_x = 0, u_y = 0, u_z = 0$$
$$w_x = 0, w_y = 0, w_z = 0$$

Figure 3. Due to the symmetry, an octant of the tissue was considered for the analysis as shown in the figure. The origin of the coordinate grid is located at the center of the cube (the bottom, back, left corner of the octant shown). The three surfaces shown in the figure are $X = 1$, $Y = 1$ and $Z = 1$. Indentation occurs at the top surface of the tissue ($Y = 1$). At the $Y = 1$ surface, everywhere except the tissue under the indenter is considered as a free boundary. By assuming an infinite tissue, or by assuming that the $X = 1$ and $Z = 1$ surfaces are attached to a rigid box, the displacements at the $X = 1$ and $Z = 1$ surfaces become zero.

For the tissue under the indenter ($Y = 1$), boundary conditions were applied by considering both intra- and extracellular spaces pressed downward (Figure 3). We assumed that the intra- and extracellular spaces of the tissue are attached to the bottom surface of the indenter, which means the displacements in the X and Z directions are equal to zero.

The depth of the indentation along the Y direction is given by δ. Therefore, when both spaces, intracellular and extracellular space, pressed downward, the boundary conditions for the space under the indenter can be written as:

$$u_x = 0, \ u_y = \delta, \ u_z = 0, \qquad w_x = 0, \ w_y = \delta, \ w_z = 0. \tag{26}$$

On the $Y = 1$ surface, we considered the area away from the indenter as a free boundary (Figure 3). Therefore, we can write the boundary conditions as:

$$\tau_{iyy} = 0, \ \tau_{iyx} = 0, \ \tau_{iyz} = 0, \qquad \tau_{eyy} = 0, \ \tau_{eyx} = 0, \ \tau_{eyz} = 0. \tag{27}$$

We can ignore the effects at the boundary of $X = 1$ and $Z = 1$ by considering an infinite tissue. Alternatively, we can assume that the tissue is attached to a rigid box. In either case, the boundary conditions for the $X = 1$ and $Z = 1$ surfaces are:

$$u_x = 0, \ u_y = 0, \ u_z = 0, \qquad w_x = 0, \ w_y = 0, \ w_z = 0. \tag{28}$$

Additional details about the boundary conditions can be found in [14].

2.3. Numerical Methods

We considered that the cube was surrounded by two layers of phantom nodes. To solve the numerical equations, we applied the overrelaxation method (an iterative method to accelerate convergence [15]) to a cube with $N \times N \times N$ nodes where $N = 45$ (including the four phantom nodes). The length of the cube (D) on each side extends from 0 to 1 ($0 < X < 1$, $0 < Y < 1$, and $0 < Z < 1$). Therefore, the space step (Δ) is 0.025. Detailed derivations of the numerical analysis and implementation can be found in the dissertation of Wijesinghe, KMGDDP [14].

The parameter ε represents the coupling strength of the two spaces. We considered $\varepsilon = 0.0001$. When the value of $\varepsilon = 0.0001$, the bidomain length constant, σ, is 0.01.

3. Results

3.1. Isotropic Tissue

Figure 4 shows the imposed boundary conditions on the extracellular space of the top surface $Y = 1$. The radius of the base of the indenter (a) is 0.25. Therefore, surface area of the bottom surface of the indenter is 0.196 (nondimensional units). The indenter is vertically displaced downward by 0.1 (nondimensional units).
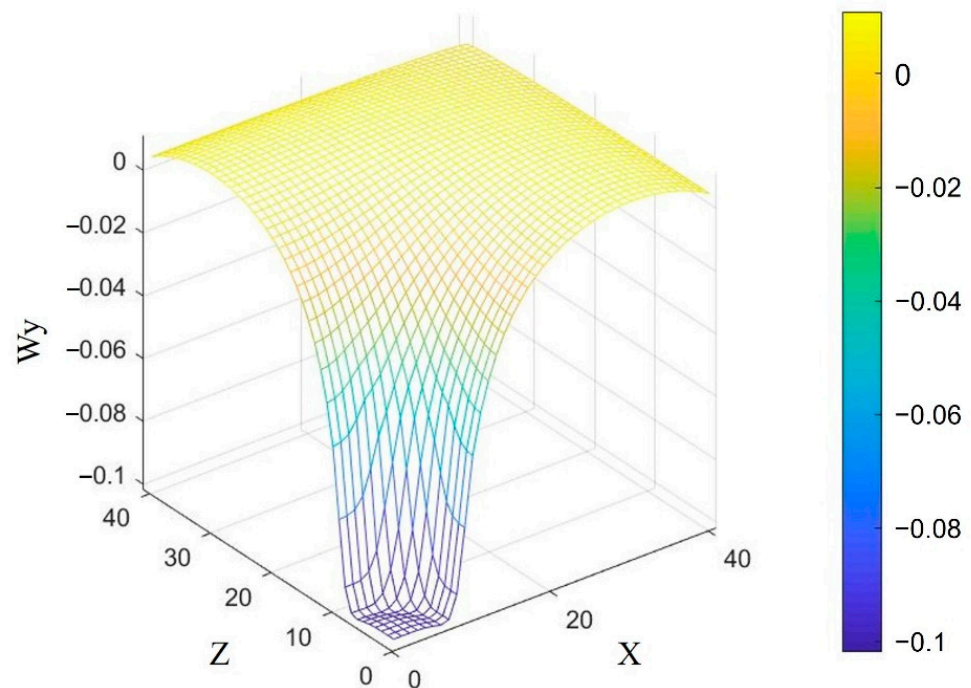

Figure 4. Displacement in the Y direction of the extracellular space, w_y, at the $Y = 1$ surface for $\varepsilon = 0.0001$.

A vector plot of the monodomain displacement is given by Figure 5. In the XZ plane, the direction of indentation is directly towards the inside of the plane along the Y direction. Displacements in XY and YZ planes are approximately 5 times larger than displacements in the XZ plane.

This analysis is particularly concerned with the bidomain displacement, because it leads to mechanotransduction. For an isotropic tissue with this boundary condition, **b** is zero. Displacements and strains (Figures 4 and 5) exist in the tissue, but there is no difference between the intracellular and extracellular displacements.

Figure 6 shows the monodomain normal and shear strains of intracellular space. The strain is localized primarily under the edge of the indenter, with some also present at the edge of the tissue.
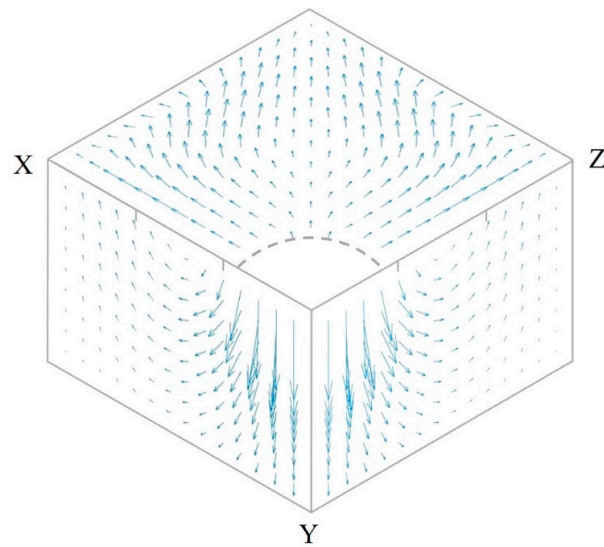
Figure 5. A vector plot of monodomain displacement **m**, for an isotropic tissue ($\gamma_i = \gamma_e = 0$). The *XZ* plane is at *Y* = 1, *XY* plane is at *Z* = 0 plane, and *YZ* plane is at *X* = 0.

ε_{ixx}

ε_{ixy}

ε_{iyy}

ε_{ixz}

ε_{izz}

ε_{iyz}
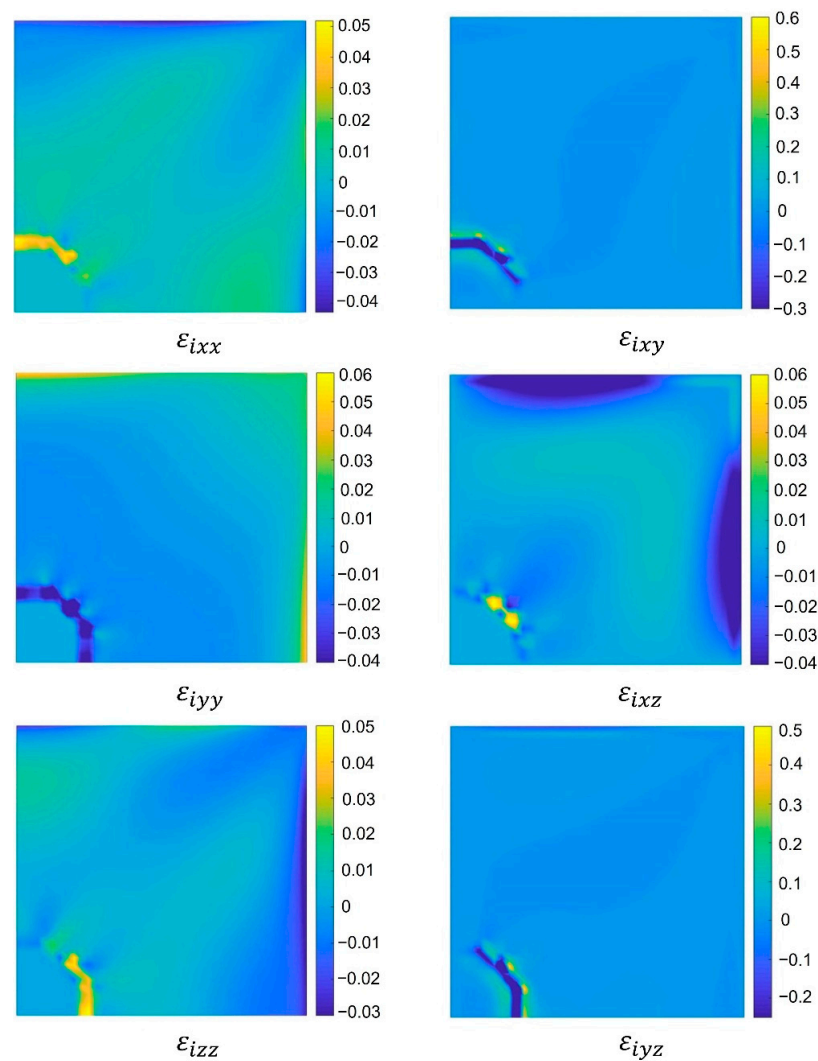
Figure 6. Monodomain normal and shear strains of intracellular space in the isotropic tissue. Each panel represents the *XZ* plane of the tissue at *Y* = 1. The fibers are horizontal.

3.2. Tissue with Equal Anisotropy Ratios

The distribution of monodomain displacement in tissue with equal anisotropy ratios is similar to the distribution of monodomain displacement in the isotropic tissue (Figure 5). The bidomain displacement remains zero for the tissue with equal anisotropy ratios.

The monodomain normal and shear strains (ε_i) of intracellular space for the tissue with equal anisotropy ratios are indistinguishable to the monodomain stains in the isotropic tissue (Figure 6).

3.3. Tissue with Unequal Anisotropy Ratios

When tissue has unequal anisotropy ratios, the monodomain displacement and intracellular monodomain strains are similar to those of Figures 5 and 6. However, bidomain displacement is no longer zero (Figure 7). The distribution of **b** is in a complicated pattern under the edge of the indenter, mainly in the direction perpendicular to the fibers.
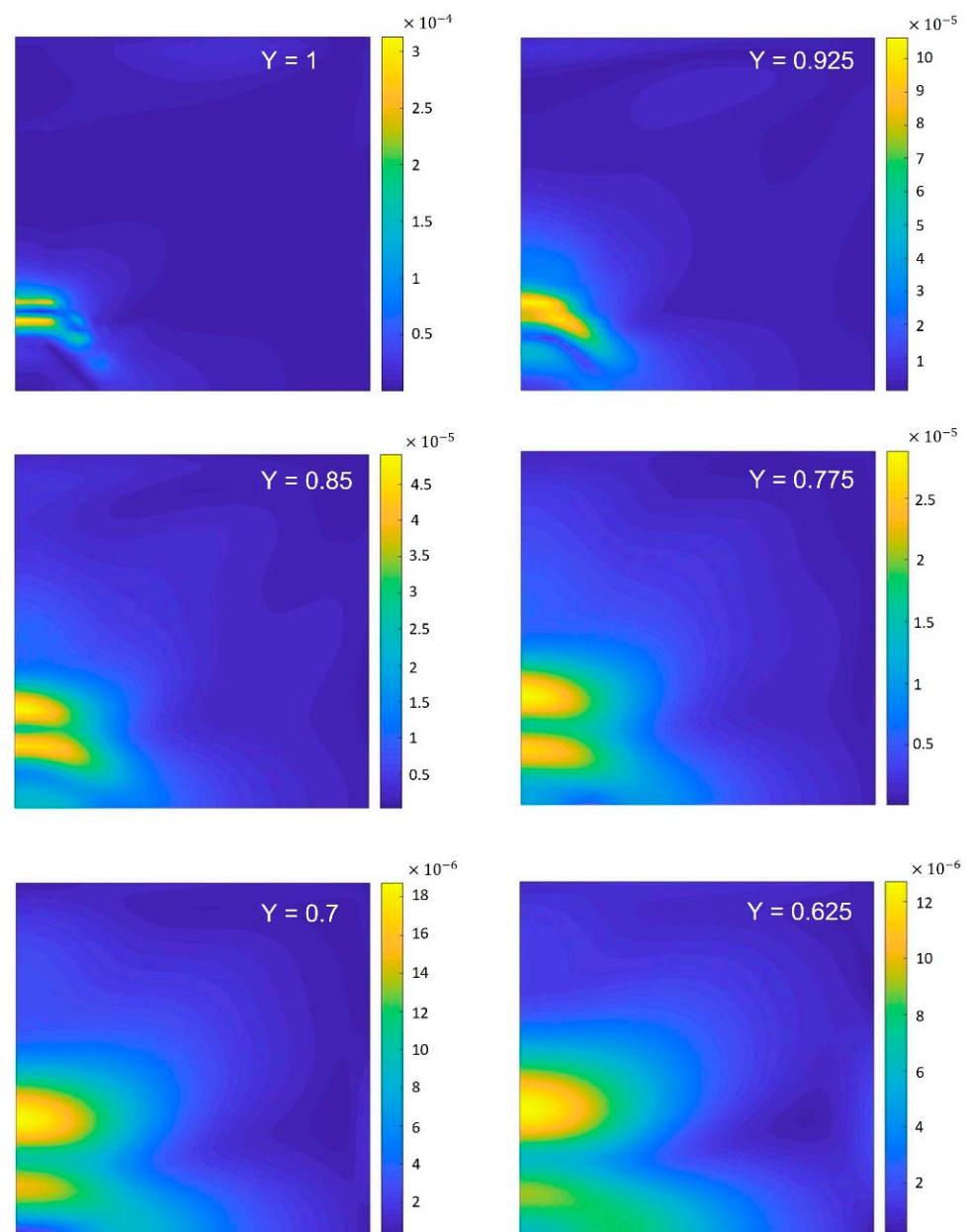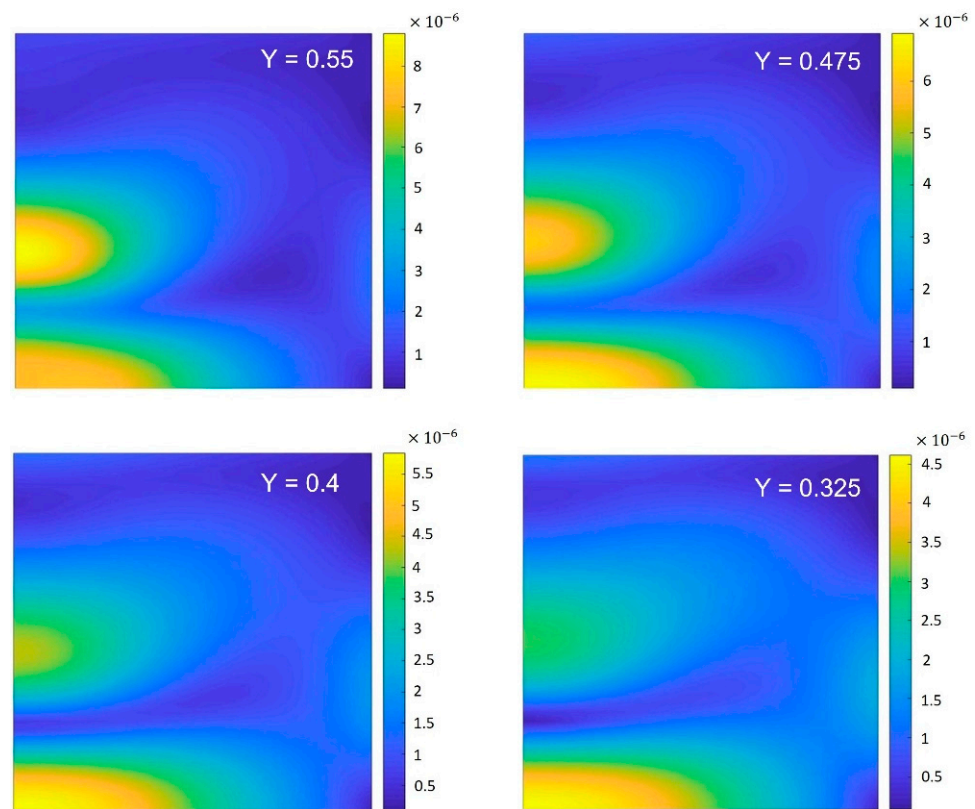

Figure 7. *Cont.*

Figure 7. Change in magnitude of bidomain displacement, **b**, in progressively deeper planes of Y for the tissue with unequal anisotropy ratios $\left(\frac{\gamma_i}{\nu} \neq \frac{\gamma_e}{\mu} \right)$. Each panel represents the XZ plane of the tissue. Tissue indentation occurs at $Y = 1$ surface. The fibers are horizontal.

Figure 8 shows the changes in the distribution of bidomain displacement for different ε values. The spatial distribution of **b** is relatively insensitive to ε, but the magnitude of **b** is roughly proportional to the square root of ε.
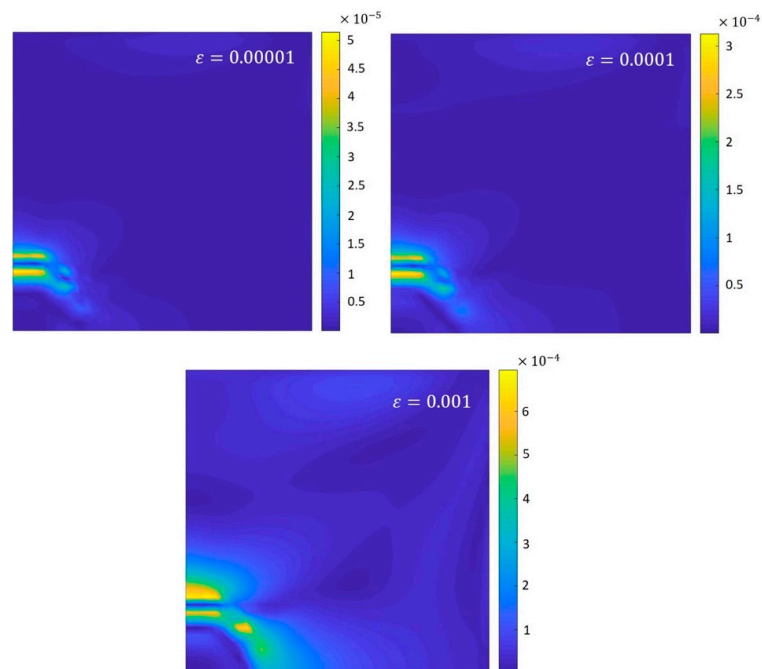
Figure 8. The magnitude of bidomain displacement, **b**, for different values of ε. The fibers are horizontal.

4. Discussion

A 3D version of the mechanical bidomain model was derived using vector potentials rather than the stream functions that are used for the 2D mechanical bidomain model [6,10,11,16]. Additionally, we defined the terms $\mathbf{m} = \mathbf{u} + \left(\frac{\mu}{\nu}\right)\mathbf{w}$ and $\mathbf{b} = \mathbf{u} - \mathbf{w}$ which helped to distinguish the monodomain and bidomain behaviors. The magnitude of bidomain displacement, $\mathbf{b}$, was important, since it represents the bidomain mechanotransduction effects in the mechanical bidomain model. In the mechanical bidomain model, effects of the direction of $\mathbf{b}$ on mechanotransduction is an open question. This study quantitatively analyzed the magnitude of the bidomain displacement, $|\mathbf{b}|$.

We used the finite difference method for the numerical analysis of the tissue indentation using the 3D mechanical bidomain model with anisotropy. Using a finite difference method for this analysis had both advantages and disadvantages. The finite difference method resulted in less complicated computational code with shorter execution time compared with using the finite element method. One major disadvantage of using the finite difference method was that we could not easily implement a variable grid spacing. A finite element approach would easily allow a smaller grid spacing near the indenter. It would also allow us to analyze irregularly shaped tissues, rather than the tissue cube we studied. Additionally, by using symmetry conditions we were able to analyze one octant of the cube, which made calculations computationally less demanding but limited the tissue geometry that we could study.

We tested the tissue by applying different boundary conditions. When free boundary conditions were applied to the outer edges of X and Z directions, the calculation became unstable and the overrelaxation routine would give large oscillations rather than converging to a solution. At large distances, the displacements of intra- and extracellular spaces $\mathbf{u}$ and $\mathbf{w}$ should go to zero regardless of outer boundary conditions. Therefore, we believed that zero displacement boundary conditions were reasonable for a large tissue. However, we had limitations for the size of the cube due to computational constraints.

The mechanical bidomain model contained pressure terms in the intracellular and extracellular spaces, p and q, which arose because the tissue was incompressible. We did not calculate p and q in our calculations, because we were focused on mechanotransduction driven by $\mathbf{b}$. We could easily have removed the pressure terms from the basic equations governing equilibrium in the tissue, Equations (7) and (8), but had a more difficult time removing the pressure from a free boundary condition (zero stress). In that case these pressure terms were removed by taking derivatives of the stress in the directions perpendicular to the surface normal, a technique explained by William H. Mitchell [17]. It would be interesting to extend our calculations to compute the pressures during tissue indentation.

We assumed linear and small strains and incompressible spaces in cardiac tissue with straight fibers. The mechanical bidomain model can also be derived for compressible spaces [18] and tissue with curving fibers [6,11].

When both intra- and extracellular spaces pressed downward, the bidomain displacement was zero in isotropic tissue and tissue with equal anisotropy ratios. However, for the tissue with unequal anisotropy ratios, the magnitude of the bidomain displacement was nonzero (Figure 7). This is because Equations (20) and (21) uncouple for isotropic and equal anisotropic tissues, but not for tissue with unequal anisotropy ratios. In 2019, Wijesinghe and Roth observed the effects of anisotropy ratios in a 2D tissue with curving fibers. They observed nonzero bidomain displacement only in tissue with unequal anisotropy ratios [6].

The issue of the appropriate boundary condition is subtle. In a study of shearing a slab of tissue [19], it was assumed that the extracellular space was being pulled, not the intracellular space. The intracellular space would also shear because it was pulled by the extracellular space, but this pulling was through the integrins coupling the two spaces, so it caused mechanotransduction at the surface. Pulling only on the extracellular space is easy to imagine (picture the tissue pulled by tiny ropes attached to the extracellular matrix). However, when pushing on tissue, it is more difficult to picture how the intracellular space

could be free. Ultimately, the correct boundary condition would need to be determined by either experiment or by a microscopic mechanical model.

We predict tissue growth as an effect of a localized force using an in vitro tissue culture experiment. This prediction needs to be tested. By growing a 3D tissue cube, pressing it down and observing over a long time, we would be able to observe how tissue grows or remodels around the area affected by the force.

We assumed that the mechanical bidomain model has unequal anisotropy ratios. Analogously, the electrical bidomain is known to have unequal anisotropy ratios. Our calculations indicate that the condition of unequal anisotropy ratios can have a dramatic effect on the distribution of mechanotransduction, but this effect is sensitive to the exact boundary condition used at the surface. This result highlights the importance of the fibrous structure of the tissue.

In comparison with the conclusions of the study conducted by Sepulveda et al., on unipolar electrical stimulation of cardiac tissue [7], our results from this study indicate that unequal anisotropy ratios can likewise affect a localized mechanical force, as in indentation. This calculation using the mechanical bidomain model is, therefore, the mechanical analogue of the Sepulveda et al.'s calculation using the electrical bidomain model. The implications of our calculation may extend beyond indentation experiments and impact any situation in which there is a localized force acting on the tissue.

In 2018, analytical expressions were derived predicting how the mechanical bidomain model responds to a localized force caused by a point source in the extracellular space [20]. This calculation, however, was for isotropic tissue. We can develop an experiment to test this phenomenon by taking a magnetic-particle based technique which is being used to activate mechanosensitive ion channels, as an example. This method allows the direct application of a highly localized mechanical force to a selected region of a mechanosensitive ion channel [21]. By inserting a superparamagnetic nanoparticle into the extracellular space, a localized force can be applied on the nanoparticle, using magnetic tweezers. This can make the nanoparticle pull the extracellular matrix, causing the integrins to stretch. The stretching of integrins in the membrane can trigger mechanotransduction [20]. The advantage of our calculation is that we could examine the influence of unequal anisotropy ratios on such an experiment.

The mechanical bidomain model was derived based on the hypothesis that the difference of the displacement of the intracellular and extracellular spaces drives the mechanotransduction. Most of the other monodomain models assume that stresses or strains cause the mechanotransduction. Macro and micro tissue indentation is a widely used technique in analyzing mechanical properties using monodomain models. From our analysis, we were able to introduce a different perspective: that tissue indentation can also affect bidomain properties. The results of this study show that the distribution of monodomain strain and distribution of bidomain displacement are qualitatively different. Therefore, to analyze the growth and remodeling of cardiac tissue, it is important to consider the forces acting on membrane integrins. The clinical significance of our results are still being determined, but our results suggest that any localized force applied to the surface of a tissue will induce growth and remodeling in a characteristic pattern around the location of the applied force.

Author Contributions: The authors performed the research together. Conceptualization, B.J.R.; Formal analysis, D.W.; Supervision, B.J.R.; Writing—original draft, D.W.; Writing—review & editing, B.J.R. All authors have read and agreed to the published version of the manuscript.

Institutional Review Board Statement: Not applicable.

Informed Consent Statement: Not applicable.

Data Availability Statement: The computer program used for this research can be found in reference [14].

Conflicts of Interest: The authors declare no conflict of interest.

References

1. Humphrey, J.D. *Cardiovascular Solid Mechanics*; Springer: New York, NY, USA, 2002.
2. Fung, Y. *Biomechanics: Mechanical Properties of Living Tissues*, 2nd ed.; Springer: New York, NY, USA, 1993.
3. Griffin, M.; Premakumar, Y.; Seifalian, A.; Butler, P.E.; Szarko, M. Biomechanical characterization of human soft tissues using indentation and tensile testing. *J. Vis. Exp.* **2016**, *118*, 54872. [CrossRef] [PubMed]
4. Singh, G.; Chanda, A. Mechanical properties of whole-body soft human tissues: A review. *Biomed. Mater.* **2021**, *16*, 062004. [CrossRef] [PubMed]
5. Pierrat, B.; MacManus, D.B.; Murphy, J.G.; Gilchrist, M.D. Indentation of heterogeneous soft tissue: Local constitutive parameter mapping using an inverse method and an automated rig. *J. Mech. Behav. Biomed. Mater.* **2018**, *78*, 515–528. [CrossRef] [PubMed]
6. Wijesinghe, D.; Roth, B.J. Mechanical bidomain model of cardiac muscle with unequal anisotropy ratios. *Phys. Rev. E* **2019**, *100*, 062417. [CrossRef] [PubMed]
7. Sepulveda, N.G.; Roth, B.J.; Wikswo, J.P. Current injection into a two-dimensional anisotropic bidomain. *Biophys. J.* **1989**, *55*, 987–999. [CrossRef]
8. Auddya, D.; Roth, B.J. A mathematical description of a growing cell colony based on the mechanical bidomain model. *J. Phys. D Appl. Phys.* **2017**, *50*, 105401. [CrossRef]
9. Sharma, K.; Roth, B.J. Engineered cardiac tissue analyzed using the mechanical bidomain model. *Phys. Rev. E* **2018**, *98*, 052402. [CrossRef]
10. Roth, B.J. The mechanical bidomain model: A review. *ISRN Tissue Eng.* **2013**, *2013*, 863689. [CrossRef] [PubMed]
11. Sharma, K.; Roth, B.J. The mechanical bidomain model of cardiac muscle with curving fibers. *Phys. Biol.* **2018**, *15*, 066012. [CrossRef] [PubMed]
12. Dong, H.; Egbert, G.D. Divergence-free solutions to electromagnetic forward and adjoint problems: A regularization approach. *Geophys. J. Int.* **2019**, *216*, 906–918. [CrossRef]
13. Jackson, J.D. *Classical Electrodynamics*, 3rd ed.; Wiley: New York, NY, USA, 1998.
14. Wijesinghe, K.M.G.D.D.P. Impacts of Anisotropy on Cardiac Mechanotransduction: Computation Based Mathematical Modeling Using the Mechanical Bidomain Model. Ph.D. Thesis, Oakland University, Rochester, MI, USA, 2021.
15. Press, W.H.; Teukolsky, S.A.; Vetterling, W.T.; Flannery, B.P. *Numerical Recipes in Fortran 77: The Art of Scientific Computing*; Cambridge University Press: Cambridge, UK, 1992.
16. Punal, V.M.; Roth, B.J. A perturbation solution of the mechanical bidomain model. *Biomech. Model. Mechanobiol.* **2012**, *11*, 995–1000. [CrossRef] [PubMed]
17. Mitchell, W.H. Exact and Numerical Solutions for Stokes Flow in Glaciers. Master's Thesis, University of Alaska, Fairbanks, AK, USA, 2012.
18. Sharma, K.; Roth, B.J. How compressibility influences the mechanical bidomain model. *Biomath* **2014**, *3*, 1–11.
19. Roth, B.J. Using the mechanical bidomain model to analyze the biomechanical behavior of cardiomyocytes. In *Cardiomyocytes: Methods and Protocols*; Skuse, G.R., Ferran, M.C., Eds.; Springer: New York, NY, USA, 2015; pp. 93–102.
20. Roth, B.J. Mechanotransduction caused by a point force in the extracellular space. *Biomath* **2018**, *7*, 1810197. [CrossRef]
21. Hughes, S.; McBain, S.; Dobson, J.; El Haj, A.J. Selective activation of mechanosensitive ion channels using magnetic particles. *J. R. Soc. Interface* **2008**, *5*, 855–863. [CrossRef] [PubMed]